

---

# Posture-dependent Human $^3\text{He}$ Lung Imaging in an Open-access MRI System: Initial Results<sup>1</sup>

Leo L. Tsai, PhD, Ross W. Mair, PhD, Chih-Hao Li, PhD, Matthew S. Rosen, PhD, Samuel Patz, PhD, Ronald L. Walsworth, PhD

---

**Rationale and Objectives.** The human lung and its functions are extremely sensitive to orientation and posture, and debate continues as to the role of gravity and the surrounding anatomy in determining lung function and heterogeneity of perfusion and ventilation. However, study of these effects is difficult. The conventional high-field magnets used for most hyperpolarized  $^3\text{He}$  magnetic resonance imaging (MRI) of the human lung, and most other common radiologic imaging modalities including positron emission tomography and computed tomography, restrict subjects to lying horizontally, minimizing most gravitational effects.

**Materials and Methods.** In this article, we review the motivation for posture-dependent studies of human lung function and present initial imaging results of human lungs in the supine and vertical body orientations using inhaled hyperpolarized  $^3\text{He}$  gas and an open-access MRI instrument. The open geometry of this MRI system features a “walk-in” capability that permits subjects to be imaged in vertical and horizontal positions and potentially allows for complete rotation of the orientation of the imaging subject in a two-dimensional plane.

**Results.** Initial results include two-dimensional lung images acquired with  $\sim 4 \times 8$  mm in-plane resolution and three-dimensional images with  $\sim 2$ -cm slice thickness.

**Conclusions.** Effects of posture variation are observed, including posture-related effects of the diaphragm and distension of the lungs while vertical.

**Key Words.** orientation; posture-dependent; lung imaging; open-access MRI; hyperpolarized  $^3\text{He}$ .

© AUR, 2008

---

The effects of body orientation and posture changes on the regional distribution of pulmonary perfusion and ventilation have been a source of renewed interest in recent years (1–4), principally because of significant questions

relating to the care and survival of patients with obstructive or restrictive lung diseases such as acute respiratory distress syndrome (3). Perfusion heterogeneity has classically been attributed to effects of gravity on pleural pressure and alveolar expansion, resulting in regional variations in lung function (5,6). Position-dependent changes in ventilation dynamics also play an important role in a variety of common clinical problems (7–9). Few methods exist that allow detailed studies of regional lung function under varying gravitational conditions—or subject orientations. Thus pulmonary physiology could benefit greatly from the development of minimally invasive methods to quantify regional lung function in subjects at variable orientations.

Magnetic resonance imaging (MRI) has only recently been recognized as a useful tool for pulmonary imaging.

---

*Acad Radiol* 2008; 15:728–739

<sup>1</sup> Harvard-Smithsonian Center for Astrophysics, 60 Garden St, MS 59, Cambridge, MA 02138 (L.L.T., R.W.M., M.S.R., R.L.W.); Harvard-MIT Division of Health Sciences and Technology, Cambridge, MA (L.L.T.); Harvard Medical School, Boston, MA (L.L.T., S.P.); Department of Physics, Harvard University, Cambridge, MA (C.-H.L., M.S.R.); Department of Radiology, Brigham And Women’s Hospital, Boston, MA (S.P.). Received July 23, 2007; accepted October 17, 2007. Support is acknowledged from NASA grant NAG9-1489, NSF grant CTS-0310006, NIH grant R21 EB006475-01A1, and Harvard University. **Address correspondence to:** R.W.M. e-mail: [rmair@cfa.harvard.edu](mailto:rmair@cfa.harvard.edu)

© AUR, 2008

doi:10.1016/j.acra.2007.10.010

Chest radiography (10) offers rapid, low-cost, high-resolution projection images with multiple subject orientations, but yields no quantitative information on gas exchange. Scintigraphy (11) offers tomographic and quantitative information but uses relatively high and costly doses of nuclear tracers and suffers from poor resolution. Computed tomography provides superior anatomic detail with limited functional data (12–14). Positron emission tomography (PET) and PET/computed tomography are used to directly measure pulmonary ventilation and perfusion and have provided the best regional quantitative detail thus far (4,15), but subjects are restricted to prone or supine orientations.

In recent years, MRI of inhaled, hyperpolarized  $^3\text{He}$  gas (16,17) has emerged as a powerful method for studying lung structure and function (18,19). This technique is used with conventional clinical MRI instruments to make quantitative maps of human ventilation (18,19), obtain regional acinar structural information via measurements of the  $^3\text{He}$  apparent diffusion coefficient (ADC) (20,21), and to monitor the regional alveolar gas-space  $\text{O}_2$  concentration ( $p_A\text{O}_2$ ) via the  $^3\text{He}$  spin-relaxation rate (22,23). These techniques have applications to basic pulmonary physiology (24) as well as lung diseases such as asthma (25,26), emphysema (20,27,28), lung cancer (27), and cystic fibrosis (29).

However, the large superconducting magnets used in conventional clinical MRI systems also restrict human subjects to lying in a horizontal orientation. Some initial studies with hyperpolarized  $^3\text{He}$  have shown that posture changes, even while horizontal, affect the lung structure modestly in a way that can nonetheless be clearly probed by  $^3\text{He}$  MRI (25,30,31). However, only minimal subject reorientation is possible inside conventional MRI scanners. An open-access MRI system that allows for different body orientations and postures has been used for studies of the lumbar spine under various loading conditions, but is even heavier and more costly than a traditional clinical MRI scanner (32–34). Also, the size, weight, and technical restrictions of traditional clinical MRI systems demand patients be brought to the scanner. For many critical care patients, the requirement of being moved from the intensive care unit is dangerous, time consuming, and expensive. Thus the potential medical benefits of hyperpolarized  $^3\text{He}$  MRI are not realized for many of the most needy patients. An open-access, lightweight, and less cumbersome MRI system, therefore, could have significant potential for monitoring critically ill lung patients.

To enable posture-dependent lung imaging, we developed an open-access MRI system based on a simple elec-

tromagnet that operates at a field strength approximately 200 times lower than a traditional clinical MRI scanner. To perform MRI at such a field strength, we exploit the practicality of hyperpolarized  $^3\text{He}$  MRI at magnetic fields  $<10$  mT (35–38).  $^3\text{He}$  hyperpolarized to 30%–60% can be created by one of two laser-based optical pumping processes (14,15) before the MRI procedure, and then high-resolution gas space imaging can be performed without the need of a large applied magnetic field. Such high-spin polarization gives  $^3\text{He}$  gas a magnetization density similar to that of water in  $\sim 10$  T fields, despite the drastically lower spin density of the gas. Thus the signal-to-noise ratio (SNR) of hyperpolarized noble gas MRI in animal or human lungs is only weakly dependent on the applied magnetic field (36), and very-low-field MRI becomes practical (36,37). In addition, after the effects of reduced magnetic susceptibility-induced background gradients and the resultant much longer  $^3\text{He}$   $T_2^*$  time at very low fields are accounted for, it can be shown that the optimum field strength for hyperpolarized  $^3\text{He}$  MRI may be around 0.1 T, not 1.5 or 3.0 T (39). In addition, operation at  $\sim 10$  mT should provide image SNR within a factor of 2–4 of that obtained in clinical scanners (39). We had previously developed a prototype open-access, very-low-field MRI system (37,38). Other groups have recognized the benefits of low-field MRI for human studies with hyperpolarized gases (40–44); however, these studies generally have employed horizontal bore MRI magnets, which restrict the subject to a single orientation (40–42,44). One study employed a vertically oriented electromagnet that allowed the subject to stand vertically, but not be imaged horizontally (43).

In this article, we present initial results on posture-dependent  $^3\text{He}$  human lung imaging obtained with our second-generation, open-access MRI system. With this system, the subject is unrestricted by the magnet and gradient coils in two dimensions. The system allows for complete reorientation of the subject into any inclined, recumbent, or inverted posture in a two-dimensional plane. Initial two- and three-dimensional human lung images are presented from subjects in two orientations—lying horizontally (supine) and sitting vertically.

## BACKGROUND

Development of an open-access MRI scanner for posture-dependent human lung imaging is motivated by:

1) current interest in the effects of body orientation and

posture changes on the regional distribution of pulmonary perfusion and ventilation and 2) the lack of existing open-access imaging technology that does not employ ionizing radiation, but does allow visualization and functional mapping of the lung in different orientations.

Regional heterogeneity of pulmonary ventilation and pulmonary perfusion is well-known to be influenced by gravity (4,45), but is also affected by the lung parenchyma and surrounding organs and stroma, leading to controversy over which effect is more physiologically relevant (5,6). Pulmonary functional residual capacity and gas elimination has been shown to be gravity-dependent (46), suggesting differences in local airway resistance. This has important clinical implications in mechanical ventilation; for example, when patients who are ventilated in a prone position tend to have improved gas exchange compared with those lying supine (1,2). Nonhorizontal orientations, such as Trendelenburg posturing, result in an increased total respiratory elastance and resistance, mainly because of decreasing lung volumes (7). The reverse Trendelenburg posture is commonly used in abdominal laparoscopic surgeries in which insufflation of the abdominal cavity is well known to have global cardiopulmonary effects from increased intraperitoneal pressure (47).

Of particular interest is the change in gas exchange dynamics when a subject is moved from a supine to an upright position. This change in orientation displaces abdominal contents inferiorly, lowering the diaphragm and distending the lungs. Ribcage motion during the breathing cycle is also increased as a result of the altered load as well as changes in respiratory muscle tone (48). Total functional residual capacity and conductance is known to significantly decrease in normal individuals undergoing such a postural change (49,50), but regional dynamics have not been measured. Although this has a small net effect on the overall respiratory mechanics of normal individuals, it can have a profound impact in disease. For example, in obese patients the total lung capacity and functional residual capacity are markedly decreased in either posture, whereas baseline airway resistance is increased and maximized in the supine state (8). Although it is generally understood that global lung mechanics are altered because of the increased load from surrounding abdominal contents and subcutaneous fat in such individuals, this provides an inadequate explanation for the observed changes in pulmonary function (9). Of similar interest is the effect of pregnancy on pulmonary dynamics, which involves not only mass effect and mechanical

changes to the cardiopulmonary circuit, but also fundamental changes to neurorespiratory drive of the mother (51). Management of such issues becomes increasingly relevant in modern medicine as the prevalence of obesity and asthma increases within the pregnant population and advances in fertility treatments allow for pregnancy at increasingly advanced maternal ages.

Regional measurements reflecting local gas dynamics and airway conductance are necessary to locate areas where the most significant physiological changes are occurring within the lung. To date, all pulmonary function tests performed on upright individuals have been via spirometry, with global resistance/conductance measurements limited to forced oscillation techniques performed at the mouth only.  $p_AO_2$ , ADC, and ventilation-perfusion ratio maps of the lung, obtained either through MRI (22,23,52) or PET (53–55) imaging, are capable of reliably resolving regional dynamics and anatomic features, but all studies have been performed on supine or prone individuals only.

The open-access magnet design of our MRI system allows for  $^3\text{He}$  lung imaging of subjects in either recumbent or upright postures. The ability to image both postures within the same system offers two major advantages: 1) comparative studies between the supine and upright state can be performed on the same instrument, eliminating a potentially major source of systematic error and 2) supine imaging with the system can be compared to the numerous supine studies already performed with PET or MRI, serving as a calibration and verification tool for the measurement techniques employed for both supine and upright lung imaging. Any gravity-dependent effects on regional lung ventilation and gas exchange seen in studies of prone and supine subjects would be further enhanced in the upright orientation, because the total vertical distance occupied by the lungs would be increased by at least 10 cm.  $^3\text{He}$  ventilation images and  $p_AO_2$  and ADC maps of the upright lung will provide previously unobtainable data pertaining to normal human lung physiology in a common, natural posture. For example, qualitative ventilation maps or quantitative measurements of  $^3\text{He}$  gas clearance over multiple breath cycles, in upright versus supine postures, will highlight regions of significant change in residual volume and resistance. These variations are likely to correlate with subject body mass index, even within normal ranges, because of mechanical and physiologic changes mentioned previously. Quantification of these changes would be a significant step toward future studies involving obese patients. The open-access design of our imager is also well-suited to image individuals with extreme

morbid obesity, whose size often excludes them from imaging via conventional PET or MRI systems.

Another important application of the open-access lung imager will be  $^3\text{He}$  MRI of asthmatic subjects. To date,  $^3\text{He}$  MRI with traditional clinical scanners have shown profound ventilation defects in supine subjects, even at an asymptomatic state (25). These defects are both transient and mobile throughout the periphery of the lung. Although asthma is classically viewed as a disease of the major central airways in which hypersensitive smooth muscles lead to obstructions in airflow, there is increasing evidence that peripheral lung involvement is also important (56–60). Supine imaging with PET has shown that ventilation defects are composed of clusters of constricted terminal bronchioles; this supports a lung branching model that possesses an intrinsic sensitivity to minor instabilities, leading to major regional patches of airway collapse (61). Importantly, such ventilation defects have usually been observed in gravity-dependent regions of the lung, so imaging in the upright posture may reveal a more exaggerated or altered distribution pattern.  $^3\text{He}$  ventilation,  $p_A\text{O}_2$ , and ADC studies on upright healthy, non-asthmatic subjects will also provide useful information, because similar, smaller-scale ventilation defects have been seen even in healthy lungs (55). Results from these studies, as well as future studies with asthmatics, will be useful not only to further understand the mechanics of airway constriction in diseases such as asthma, but also to help understand how and why inhaled therapeutics, usually administered with the patient in an upright posture, can be effective for some patients but not for others, and how coexisting conditions such as obesity can complicate management.

The quality of life among the ever-growing geriatric population is often reduced by dyspnea, which generally results from age-related changes in pulmonary function. Anatomic and physiologic changes in older lungs include smaller airway size, increased peripheral airway resistance leading to air trapping, and increasing pulmonary compliance—characteristics that can be emphysema-like (62). Some of these alterations can be present by age 40, even among healthy individuals. Although total lung capacity remains fairly constant with age, inspiratory and expiratory residual volumes increase while tidal volume decreases, exacerbating regional air trapping in the periphery (63,64).  $^3\text{He}$  ADC,  $p_A\text{O}_2$ , and ventilation imaging of healthy adults with an open-access MRI system is expected to reveal age-dependent regional changes in airway dimensions and ventilation defects from peripheral bron-

chiole airway closure and may show an association between some of those changes and subject age. Equally important is the study of how and to what extent these changes are influenced by postural variations—an investigation that would be possible with an open-access MRI system. Such data would help elucidate, for example, how some healthy elderly patients who do not have classic sleep apnea can experience respiratory discomfort while lying supine but significantly alleviate their symptoms in a slight reverse Trendelenburg orientation. This study may also be influential in the intensive care setting, where mechanical ventilation in geriatric patients is often associated with poorer outcomes (65). Potential studies involving geriatric patients would be further aided by an open-access MRI system operating at very low magnetic field, which would allow easier access than a traditional clinical scanner for disabled patients, as well as those with metallic or electronic implants who would be excluded from traditional clinical MRI systems.

Finally, idiopathic pulmonary hypertension is a public health problem of increasing interest (66). This disease is typically discovered around the fourth decade, after complaints of dyspnea at rest or with minor activity. However, ventilation-perfusion ratio mismatches can manifest themselves symptomatically under heavy exercise stress (eg, in high-performance athletes) up to two decades earlier. In the case of chronic thromboembolic pulmonary hypertension (67), subjects suffer multiple microscopic, radiographically invisible pulmonary embolisms that can eventually lead to clinical symptoms of pulmonary hypertension. The initial clinical picture can mimic early idiopathic pulmonary hypertension, in which symptoms become apparent only with major exercise. Suspicion of chronic thromboembolic pulmonary hypertension requires a stress exercise test in which patients are monitored invasively with pulmonary arterial catheters and real-time blood gas analysis (68). An open-access MRI system, which would permit patients to undergo an exercise challenge while inside the MRI scanner and then be monitored in a noninvasive manner, including local measurements of  $\text{O}_2$  distribution and consumption, would be a significant improvement in the study of the progression of this disease.

## EXPERIMENTAL

### Imager Design

A detailed description of the design and operation of our open-access human MRI system, refined from the

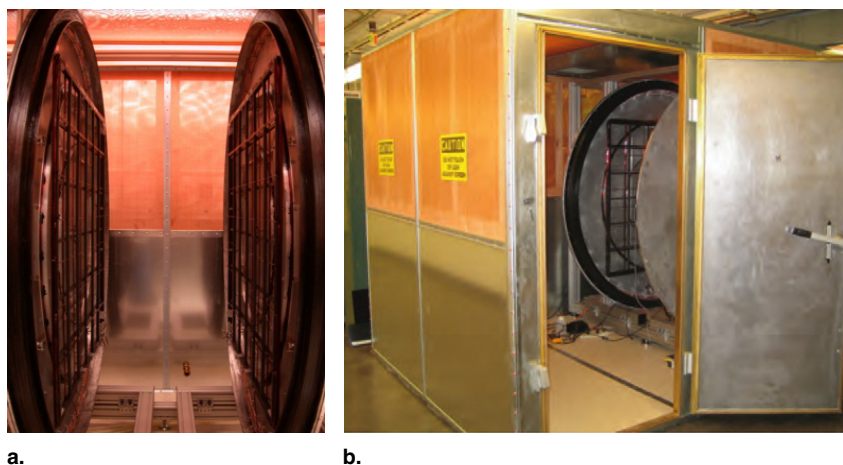


**Figure 1.** Photographs of the open-access human magnetic resonance imaging system. **(a)** The open-access imaging area, which allows reorientation of a subject. The gap between the two coils is 90 cm, with more than 2 meters of open space in the other two dimensions. The photograph shows the pair of main  $B_0$  coils on their aluminum support flanges, with the gradient coils located parallel to each  $B_0$  coil on additional supports bolted to the flanges. **(b)** The entire imager on its customized aluminum framework, located inside an RF-shielded room. Access to the imaging region from outside the room is straightforward.

prototype imager (37,38), will be presented elsewhere (69). Here, a brief overview of the design and how it permits variable-posture lung imaging is provided.

The imager operates at an applied static magnetic field,  $B_0$ , of 6.5 mT (65 G). The  $B_0$  field is created by a four-coil, biplanar magnet design (70) with pairs of coils measuring 2 and 0.55 meters in diameter. One large and small coil are mounted together on a 2.2-meter diameter aluminum flange. There are two of these flange and coil sets, which are wound and arranged in a mirroring fashion, and are mounted vertically on a customized stand made of extruded aluminum beams, maintaining a separation of  $\sim 90$  cm between coil sets (Fig 1a). All four coils are connected in series to a single DC power supply that supplies 42.2 A of current to reach the desired  $B_0$  of 6.5 mT. This field allows  $^3\text{He}$  MRI at a frequency of 210 kHz. With manual shimming and DC offsets on the gradient coils, the magnetic field exhibits a total variation of less than  $\sim 5 \mu\text{T}$  (350 ppm) across the volume of a human chest, which allows  $^3\text{He}$  NMR signals from such volumes with spectral full-width half maximum (FWHM) line widths of  $\sim 30$  Hz.

Planar gradient coils were built to provide the pulsed magnetic field gradients, thus eliminating another restrictive cylindrical geometry found in clinical MRI scanners. The coils were designed to allow the acquisition of  $256 \times 256$   $^3\text{He}$  images across a 40-cm

field of view with an imaging bandwidth of 10 kHz, while minimizing concomitant field effects (71). We wound the coils using insulated magnet wire on nonconducting, freestanding frames to facilitate heat dissipation and minimize eddy current formation in the  $B_0$  coil/flange structure. The  $z$  coils consist of two sets of three circular loops, with each set mounted on the magnet flange, parallel to the  $B_0$  coils. The  $x$  and  $y$  gradients consist of freestanding rectangular grids mounted on each magnet flange (Fig 1a), maintaining the  $\sim 90$  cm spacing for subject access. The gradient coils are powered by Techron 8607 gradient amplifiers, operating at up to 140 A. At maximum current, the three gradients each provide  $\sim 0.07$  G/cm gradient strength with a 500- $\mu\text{s}$  rise time.

RF frequency and gradient control is accomplished using a Tecmag Apollo commercial MRI research console (Tecmag Inc, Houston, TX). This system is designed to operate at frequencies as low as 100 kHz without further hardware modification, unlike traditional MRI scanners. RF pulses from the Apollo are fed to an NMR Plus 5LF300S amplifier (Communications Power Corp Inc, Hauppauge, NY), which provides up to 300 W of RF power. We employed a single RF coil for  $B_1$  transmission and detection in conjunction with a Transcoupler II probe interface-T/R switch (Tecmag) optimized for 200-kHz operation. The RF coil is a large solenoid designed to accommodate the subject's shoulders and arms and com-

pletely cover the thoracic region. The coil is  $\sim 50$  cm in diameter and length and is tuned to 210 kHz using an external capacitive resonance box that is remote from the coil. At maximum power, the  $90^\circ$  hard pulse has a duration of  $\sim 300$   $\mu\text{s}$ . Being a solenoid, the coil has very high  $B_1$  homogeneity (69) and can be rotated along with the subject in the imaging plane, while remaining perpendicular to the direction of  $B_0$ . The coil has a quality factor  $Q \sim 30$ , implying operating bandwidths of  $\sim 10$  kHz at the  $^3\text{He}$  Larmor frequency of 210 kHz. This low coil  $Q$  removes the effect of the coil response function being convolved with the image dataset, as we had seen previously with coils of higher  $Q$  and lower Larmor frequencies (38). At a Larmor frequency of 210 kHz, the human body does not affect the coil  $Q$  and has minimal loading effects, allowing the RF coil power and flip angles to be calibrated ahead of time and remain reproducible from subject to subject, unlike the case for operation at  $>10$  MHz frequencies in traditional clinical MRI scanners.

To improve SNR, the  $B_0$ , gradient and  $B_1$  coils were housed inside an RF-shielded room (Lindgren RF Enclosures Inc, Glendale Heights, IL) (Fig 1b). The room attenuates environmental RF interference in the range of 10 kHz to 10 MHz by up to 100 dB. Power lines for the  $B_0$  magnet, preamplifier, and RF coil connections all pass through commercial filters that shield out noise higher than 10 kHz (Lindgren Inc.). The gradient lines pass into the shielded room via three sets of custom high-current passive line filters that produce  $\sim 25$  dB attenuation at 100 kHz (Schaffner Inc, Luterbach, Switzerland).

### MRI Techniques

We employed standard two- and three-dimensional fast gradient-recalled echo sequences for image acquisition. To efficiently use the nonrenewable magnetization from hyperpolarized  $^3\text{He}$ , low-flip-angle excitation pulses were used throughout (72). Two-dimensional (2D) projection images were acquired without slice selection, using an excitation flip angle of  $\sim 5^\circ$ , dataset size of  $128 \times 64$  points, and  $50 \times 50$ -cm field of view in  $\sim 5$  seconds. Three-dimensional (3D) images were acquired by repeating the 2D experiment with six different third-dimension phase encoding gradients alternating in a centric manner (73–75). These experiments yielded a 3D dataset of size  $128 \times 64 \times 6$  across a field of view of  $50 \times 50 \times 12$  cm, using an excitation flip angle of  $\sim 4^\circ$ , acquired in  $\sim 30$  seconds. All imaging acquisitions used the following parameters: bandwidth = 4.0 kHz, 2.2 milliseconds sinc-shaped RF pulse, echo time/repetition time

$\sim 29/86$  milliseconds, NEX = 1. The datasets were zero-filled to  $128 \times 128$  (2D) or  $128 \times 128 \times 8$  (3D) points before fast-Fourier transformation.

### Polarized $^3\text{He}$ Production and Delivery

Hyperpolarized  $^3\text{He}$  gas is produced via the spin-exchange optical pumping technique using vaporized Rb as an intermediate (14). Our modular  $^3\text{He}$  polarization apparatus includes gas storage, transport, and delivery stages (37); recent modifications are described here. The polarization cells are  $\sim 80$   $\text{cm}^3$  in volume and made of Pyrex glass. A magnetic field of  $\sim 2.3$  mT is generated by a five-coil arrangement mounted on the polarizer, thereby providing a quantization axis for optical pumping. The 2.3-mT field also allows in situ polarization monitoring via NMR detection at a Larmor frequency of 74 kHz using a benchtop Aurora spectrometer (Magritek, Wellington, New Zealand). The polarizer is located adjacent to, but outside, the RF-shielded room. For each experiment, we filled a polarization cell with  $\sim 5$ – $6$  bar of  $^3\text{He}$  and 0.1 bar of  $\text{N}_2$ , heated the cell to  $\sim 170^\circ\text{C}$ , and applied  $\sim 30$  W of circularly polarized light at 794.7 nm, provided by a line-narrowed diode laser apparatus that has an intense spectral output at  $794.7 \pm 0.1$  nm (Spectra Physics Inc, Tucson, AZ).

After spin-exchange optical pumping for  $\sim 8$ – $10$  hours, the  $^3\text{He}$  nuclear spin polarization reaches  $\sim 20\%$ – $40\%$ . We then expand the polarized gas from the optical pumping cell into a previously evacuated glass and Teflon compressor for storage and delivery. The polarized  $^3\text{He}$  is then delivered via Teflon tubing through a feed through in the RF shielded room to a delivery manifold adjacent to the subject. This manifold consists of a Tedlar bag, vacuum and inert gas ports, and a Teflon tube through which the gas is inhaled. The valves on the manifold are controlled pneumatically.

### Human Imaging Protocol

Figure 2 shows subjects in the open-access imager in both horizontal and vertical orientations. After a relaxed expiration, the subjects inhale, through the Teflon tubing,  $\sim 500$   $\text{cm}^3$  of hyperpolarized  $^3\text{He}$  gas, usually followed by a small breath of air to wash the helium out of the large airways and distribute it throughout the lung. The MRI sequence begins immediately after inhalation and proceeds while the subject maintains a breathhold for 30–40 seconds. We monitor the subject's heart rate, blood pressure, and blood oxygen saturation throughout. Subjects were restricted to healthy adults between 18 and 60 years

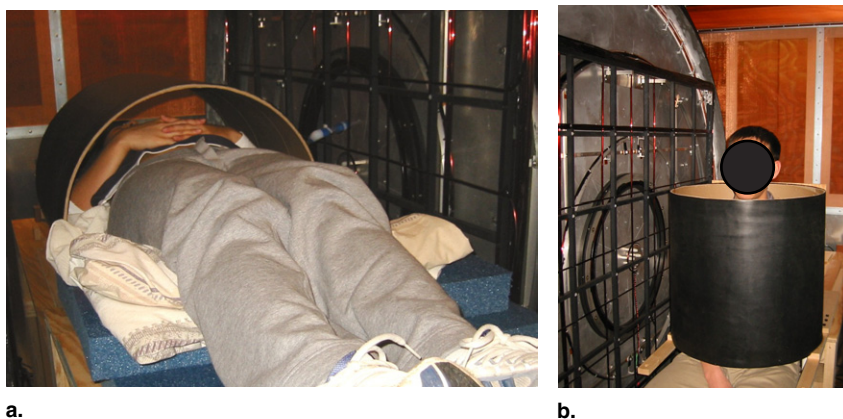


**Figure 2.** Subjects in the open-access human magnetic resonance imaging system. **(a)** Subject on the support table, ready for imaging in the supine position. The  $B_1$  coil is slid into position with the aid of positional guides on the table, below the subject support bed. **(b)** Subject sitting on a wooden chair, ready for vertical orientation imaging. The  $B_1$  coil is raised and lowered with a wooden support mechanism that allows easy positioning of the subject and ensures the coil returns to the correct position, independent of the subject.

of age, with body mass index  $<30$ , a resting blood oxygen saturation  $>95\%$ , and no history of pulmonary or cardiologic disease. All human experiments are performed according to a protocol approved by the Partners Human Research Committee at Brigham and Women's Hospital/Massachusetts General Hospital, under an interinstitutional institutional review board agreement with the Harvard University Committee for the Use of Human Subjects. A Food and Drug Administration Investigational New Drug was not required for this study.

## RESULTS AND DISCUSSION

As can be seen in the photographs in Fig 2, the imager easily accommodates subjects in the supine and vertical orientations without being significantly encumbered or having their posture influenced by the RF coil. Figure 3 shows example 2D human  $^3\text{He}$  MRI lung images, acquired without slice selection in the open-access human MRI system, operating at a field strength of 6.5 mT. Both images have a coronal orientation, with the lungs viewed in an anteroposterior direction (ie, the subject's right lung is on the left side of the images). The images exhibit both an absence of artifacts and high SNR. SNR varies from  $\sim 25$  to 80 (Fig 3a) and  $\sim 50$  to 140 (Fig 3b). The images were obtained without using a variable flip angle for reproducible transverse magnetization from each successive RF pulse (72), because the excitation flip angle was sufficiently low to ensure minimal variation in magnetization

over the first  $\sim 50$  phase-encoding rows, and hence produce an artifact-free image. The in-plane resolution in both images is  $\sim 4 \times 8$  mm.

The horizontal image (Fig 3a) shows the two lungs with the usual concave shape at the bottom as the diaphragm pushes against the lungs. Because this image did not employ slice selection, the boundary is not sharp, but rather shows that the diaphragm impacts the front portion of the lower lung, while the lungs extend down below the diaphragm at the back. A region of lower intensity in the middle region of the left lung is consistent with the location of the heart and major aorta. The gas distribution is uniform throughout the two lungs, as expected for a healthy subject with low body mass in this orientation. The vertical image (Fig 3b) shows modest distension of the lungs in this same subject. Also, in the vertical orientation, the effect of the diaphragm on the lower portion of the lung is clearly absent. The helium gas distribution remains highly uniform, and a small trace of gas can be observed in the trachea and major bronchi.

The main application of the open-access imager is posture-dependent functional lung studies (eg,  $p_{\text{A}}\text{O}_2$  mapping), which relies on accurately measuring MRI signal attenuation as a function of time. In such measurements, the use of narrow slice-selective imaging methods can lead to reduced accuracy in quantitative data because out-of-slice magnetization can diffuse into the image slice during the pulse sequence and interimage delays and so result in an apparent signal attenuation that is lower than

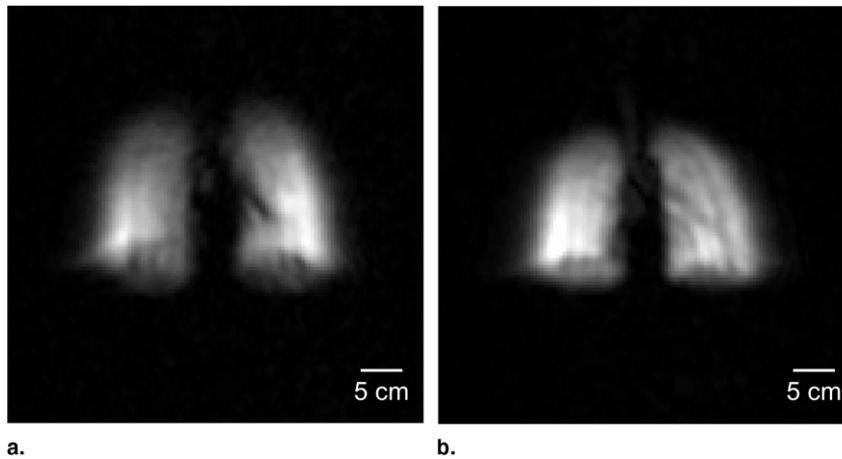


**Figure 3.** Two-dimensional projection  $^3\text{He}$  human magnetic resonance imaging (MRI) of human lungs, obtained using the open-access human MRI system, with subjects positioned as shown in Fig 2. **(a)** Image obtained while the subject was lying horizontally in a supine orientation. **(b)** Image acquired while the subject was sitting vertically. Both images visualize the lungs as if looking at the subject from the front (ie, the subject's right lung lobe is on the left of the image). Imaging parameters:  $B_0 = 6.5$  mT, Larmor frequency = 210 kHz, field of view = 50 cm, NEX = 1, flip angle =  $5^\circ$ , echo time/repetition time = 28.5/85.8 milliseconds. Data size =  $128 \times 64$ , zero-filled to  $128 \times 128$ , total scan time  $\sim 4$  seconds.

would be expected because of the measurement alone (73–75). This can result in underestimations of  $p_A\text{O}_2$  by as much as factor of four (75). We note that early  $p_A\text{O}_2$  mapping was also performed using projection images, partly for this reason (22,52), whereas recent studies incorporating slice selection have used only one or a few slices (23,76), followed by binning of multiple pixels together for analysis. In addition to avoiding thin-slice selection methods for  $p_A\text{O}_2$  mapping, multislice experiments become more difficult to implement at the much lower RF frequencies used in the open-access imager than at the higher frequencies used in traditional clinical scanners. Generally, slices away from the magnet isocenter are achieved by varying the frequency of the slice-selective RF pulse by an amount proportional to the distance of the center of the slice from the magnet center. This frequency offset is usually in the range of  $\sim 1$ –10 kHz. At a Larmor frequency of 210 kHz, and with a coil  $Q$  of  $\sim 30$ , the coil response has a frequency width of  $\sim 10$  kHz. Therefore frequency offsets of anything more than a couple of kilohertz would significantly attenuate the RF pulse received by the sample, and any slice selection away from the magnet isocenter would result in variable RF calibrations.

For these reasons, we have not implemented slice selection in 2D imaging methods and have instead used 3D phase encoding to spatially resolve the lung in the third dimension. Figures 4 and 5 show example 3D lung image

datasets acquired with the open-access imager. Figure 4 was acquired while the subject was horizontal, in the supine position, whereas Fig 5 was acquired with a different subject sitting vertically. Both figures show multiple image planes of  $\sim 2$  cm thickness, displaying the images in the anteroposterior view, and from anterior to posterior in the image montage (#1–8).

The 2D image planes of Fig 4 define the edges of the lungs and show an even distribution of  $^3\text{He}$  throughout the periphery. The regions exhibiting the greatest anteroposterior thickness correspond to the regions of greatest intensity signal from the 2D projection image. Anterior planes #2–4 show the cardiac cavity and also illustrate the characteristic concave curvature from the diaphragm, which is absent from the posterior planes #6–8. The central planes also show a faint  $^3\text{He}$  signal in the left bronchus, but not in the right one. We attribute this to residual  $^3\text{He}$  remaining in the large airways even after the subject had taken a chaser breath of room air. This is consistent with anatomy; the left bronchus has a slightly sharper branching angle and thus gas flow through that region is lower in comparison to the right bronchus. Despite the use of the 3D phase encoding, the image SNR in each plane remains high, generally around 40–60 for planes #3–6 and  $\sim 15$ –30 for the peripheral planes.

For the 3D image of Fig 5, the subject did not take an additional breath of room after their inhalation of the sup-

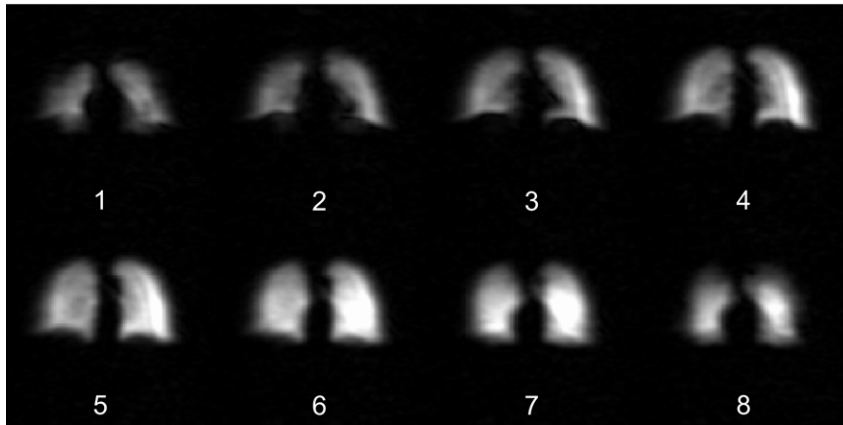


**Figure 4.** Three-dimensional  $^3\text{He}$  magnetic resonance image series of human lungs, obtained using the open-access human MRI system, with subject lying horizontally in a supine orientation. All planes visualize the lungs as if looking at the subject from the front (ie, the subject's right lung lobe is on the left of the image). Image planes represent slices  $\sim 1.5\text{-cm}$  thick, and progress from anterior (#1) to posterior (#8) through that dataset. Imaging parameters:  $B_0 = 6.5\text{ mT}$ , Larmor frequency = 210 kHz, field of view =  $50 \times 50 \times 12\text{ cm}$ , NEX = 1, flip angle =  $4^\circ$ , echo time/repetition time = 28.5/85.8 milliseconds. Data size =  $128 \times 64 \times 6$ , zero-filled to  $128 \times 128 \times 8$ , total scan time  $\sim 30$  seconds.

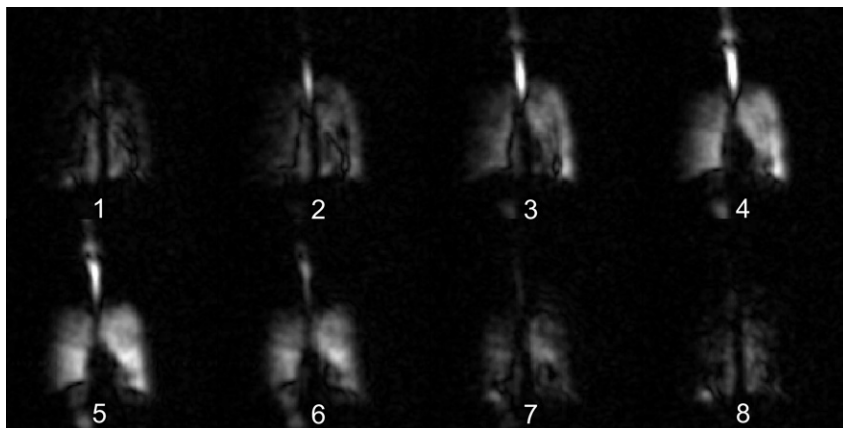


**Figure 5.** Three-dimensional  $^3\text{He}$  magnetic resonance imaging (MRI) series of human lungs, obtained using the open-access human MRI system, with subject positioned vertically. Additional room air was not inhaled after  $^3\text{He}$  inhalation, resulting in nonuniform  $^3\text{He}$  distribution throughout the lung, and intense signal in the trachea and oral cavity. MRI signal below the diaphragm in each image, beside the plane number, is most likely from gas above the trachea and outside the top of the image field of view that was folded in to the bottom portion of the image. Image orientation, layout, and acquisition parameters are the same as for Fig 4.

plied helium. As a result, the 2D image planes show intense signal from  $^3\text{He}$  gas in the oral cavity and upper airways, whereas the gas is not uniformly distributed in the lungs. A number of thin dark lines branch out from a central location in the left lung (shown on the right), where the pulmonary outflow originates. These lines could, therefore, be larger blood vessels that are visualized more easily when in the vertical position, or they

could result from motion artifacts because of the effects of cardiac motion on the lung tissue during a breathhold. There is also the possibility of 3D truncation artifacts given the use of a 12 cm field of view in the third dimension, despite the fact our subjects inhaled only  $500\text{ cm}^3$  of helium gas and were therefore well below maximum lung capacity when imaged. Because the images were acquired with centric phase encoding in 3D, we do not believe

$k$ -space filtering from magnetization loss was significant. We note these are preliminary results from this novel imager, and such features in the images will be investigated thoroughly in the future.

We emphasize two significant benefits of performing pulmonary MRI at low  $B_0$  and Larmor frequency. First, we operate well below the frequency range in which “sample noise” dominates human MRI (36,38). Thus we found that placing the RF coil over the subject resulted in minimal coil loading effects in comparison to an empty coil. The coil  $Q$  was not affected in any way by the presence of the subjects, and the coil resonance moved a very small and reproducible amount (69). In addition to making sample noise insignificant, this effect eliminates tuning/matching errors and variation in RF pulse calibrations from subject to subject. Second, we can use an open biplanar electromagnet to create a horizontal  $B_0$  and thereby allow a solenoid RF coil to be used, which can then be rotated with the subject through various postures (Fig 2). In addition to being the most sensitive RF detectors, solenoidal coils have the most homogeneous  $B_1$  field among common RF coil designs (77). Therefore a significant confounding step in pulmonary functional imaging methods such as  $p_A\text{O}_2$  mapping (ie, the need to calibrate the effect of RF flip angle effects on a pixel-by-pixel basis for every trial with every subject (22,23,52)), may not be necessary in our open-access imager. Instead, it will be possible to calibrate the RF coil pulse power in advance using appropriate phantoms (69) and apply this known value to later image post-processing procedures.

Finally, we note that the images presented here were acquired with a readout gradient of  $\sim 0.5$  mT/m (0.05 G/cm), which is an order of magnitude lower than values used in traditional clinical MRI scanners. At large  $B_0$ , gradients of  $\sim 10$  mT/m are employed to enable rapid echo acquisition ( $\sim 5$ – $10$  milliseconds per row), and, specifically for pulmonary imaging, to ensure that the pulsed gradient fields dominate the susceptibility-induced background gradient fields in the human lung, which scale with  $B_0$ . When operating at much lower  $B_0$ , the need for large readout gradients to dominate background gradients is no longer relevant. Additionally, use of low gradient strengths ensure that the maximum gradient across the sample, and hence gradient deviation from linearity, remains low in comparison to  $B_0$ , minimizing concomitant field effects (71). However, when using such low-strength encoding gradients, correspondingly longer echo acquisition and repetition times must be used in order to achieve image resolution comparable to that obtained with tradi-

tional clinical MRI scanners. This, in turn, reduces image temporal resolution. A straight-forward step to increase gradient strength, and so improve image temporal resolution, is to operate the gradient current amplifiers in series to double the maximum current available to the gradient coils. The design of the coils is not limited to a given current and will support significantly higher currents than those used in the system’s present configuration. Modification to the design of the gradient coils could also double the gradient strength. Such steps could improve temporal resolution by a factor of 4, while still ensuring the overall field gradient is low enough to avoid image distortion due to concomitant field effects (71).

## CONCLUSION

We have demonstrated human lung imaging in both the horizontal and vertical body orientations using inhaled hyperpolarized  $^3\text{He}$  gas and an open-access MRI instrument operating at an applied magnetic field of 6.5 mT (65 G). Two- and three-dimensional coronal lung images in the anteroposterior view were obtained during  $^3\text{He}$  breath-holds. 2D images were obtained without slice selection, whereas 3D images yielded six image planes with a thickness of  $\sim 2$  cm. In-plane image resolution was  $\sim 4 \times 8$  mm. Peak SNR is high, being  $\sim 100$  for the 2D projection images, and more than 30 for the planes of the 3D data-sets. The images show differences in lung shape and size as a function of subject posture, which indicates that the open-access imager will enable posture-dependent pulmonary functional imaging and thereby serve as a valuable tool for the study of critical pulmonary diseases and questions relating to posture-dependent and gravitational effects on pulmonary function. In addition, the open-access imager, operating such a low applied field, could provide lung imaging for subjects with implants, prostheses, claustrophobia, or acute illnesses who have been denied access to MRI in its traditional form.

## ACKNOWLEDGMENTS

We thank Dr. Mirko Hrovat, Dr. Jim Maddox, Ms. Rachel Burke, Ms. Ana Batrachenko, Ms. Rachel Scheidegger, and Mr. Dan Chonde for technical assistance with imager, and Dr. Michael Barlow for assistance with the novel laser source. We are indebted to Kenneth Tsai, MD, who acted as observing physician for human imaging trials, and George Topulos, MD, who devised the human protocols.

## REFERENCES

- Mure M, Domino KB, Lindahl SGE, et al. Regional ventilation-perfusion distribution is more uniform in the prone position. *J Appl Physiol* 2000; 88:1076-1083.
- Mure M, Lindahl SGE. Prone position improves gas exchange—but how? *Acta Anaesthesiol Scand* 2001; 45:150-159.
- Gattinoni L, Tognoni G, Pesenti A, et al. Effect of prone positioning on the survival of patients with acute respiratory failure. *N Engl J Med* 2001; 345:568-573.
- Musch G, Layfield JD, Harris RS, et al. Topographical distribution of pulmonary perfusion and ventilation, assessed by PET in supine and prone humans. *J Appl Physiol* 2002; 93:1841-1851.
- Glenny RW, Lamm WJ, Albert RK, et al. Gravity is a minor determinant of pulmonary blood flow distribution. *J Appl Physiol* 1991; 71:620-629.
- West JB, Hlastala MP. Importance of gravity in determining the distribution of pulmonary blood flow. *J Appl Physiol* 2002; 93:1888-1891.
- Fahy BG, Barnas GM, Nagle SE, et al. Effects of Trendelenburg and reverse Trendelenburg postures on lung and chest wall mechanics. *J Clin Anesth* 1996; 8:236-244.
- Yap JC, Watson RA, Gilbey S, et al. Effects of posture on respiratory mechanics in obesity. *J Appl Physiol* 1995; 79:1199-1205.
- Watson RA, Pride RB. Postural changes in lung volumes and respiratory resistance in subjects with obesity. *J Appl Physiol* 2005; 98:512-517.
- Potchen EJ, Cooper TG, Sierra AE, et al. Measuring performance in chest radiography. *Radiology* 2000; 217:456-459.
- Taplin GV, Poe ND. A dual lung-scanning technique for evaluation of pulmonary function. *Radiology* 1965; 85:365-368.
- Mayo JR, Webb WR, Gould R, et al. High-resolution CT of the lungs—an optimal approach. *Radiology* 1987; 163:507-510.
- Jones AR, Hansell DM, Evans TW. Pulmonary perfusion in supine and prone positions: an electron-beam computed tomography study. *J Appl Physiol* 2001; 90:1342-1348.
- Saba OI, Chon D, Beck K, et al. Static versus prospective gated non-breath hold volumetric MDCT imaging of the lungs. *Acad Radiol* 2005; 12:1371-1384.
- Layfield D, Venegas JG. Enhanced parameter estimation from noisy PET data: part I—methodology. *Acad Radiol* 2005; 12:1440-1447.
- Walker TG, Happer W. Spin-exchange optical pumping of noble-gas nuclei. *Rev Mod Phys* 1997; 69:629-642.
- Nacher PJ, Leduc M. Optical pumping in  $^3\text{He}$  with a laser. *J Physique* 1985; 46:2057-2073.
- Leawoods JC, Yablonskiy DA, Saam B, et al. Hyperpolarized  $^3\text{He}$  gas production and MR imaging of the lung. *Concepts Magn Reson* 2001; 13:277-293.
- Moller HE, Chen XJ, Saam B, et al. MRI of the lungs using hyperpolarized noble gases. *Magn Reson Med* 2002; 47:1029-1051.
- Salerno M, de Lange EE, Altes TA, et al. Emphysema: hyperpolarized helium 3 diffusion MR imaging of the lungs compared with spirometric indexes—initial experience. *Radiology* 2002; 222:252-260.
- Saam BT, Yablonskiy DA, Kodibagkar VD, et al. MR imaging of diffusion of  $^3\text{He}$  gas in healthy and diseased lungs. *Magn Reson Med* 2000; 44:174-179.
- Deninger AJ, Eberle B, Ebert M, et al. He-3-MRI-based measurements of intrapulmonary  $p(\text{O}_2)$  and its time course during apnea in healthy volunteers: first results, reproducibility, and technical limitations. *NMR Biomed* 2000; 13:194-201.
- Rizi RR, Baumgardner JE, Ishii M, et al. Determination of regional  $V_A/Q$  by hyperpolarized  $^3\text{He}$  MRI. *Magn Reson Med* 2004; 52:65-72.
- Mills GH, Wild JM, Eberle B, et al. Functional magnetic resonance imaging of the lung. *BJA: Brit J Anaesth* 2003; 91:16-30.
- Altes TA, Powers PL, Knight-Scott J, et al. Hyperpolarized  $^3\text{He}$  MR lung ventilation imaging in asthmatics: preliminary findings. *J Magn Reson Imag* 2001; 13:378-384.
- Samee S, T. Altes TA, Powers P, et al. Imaging the lungs in asthmatic patients by using hyperpolarized helium-3 magnetic resonance: assessment of response to methacholine and exercise challenge. *J Allergy Clin Immunol* 2003; 111:1205-1211.
- Kauczor HU, Ebert M, Kreitner KF, et al. Imaging of the lungs using  $^3\text{He}$  MRI: preliminary clinical experience in 18 patients with and without lung disease. *J Magn Reson Imaging* 1997; 7:538-543.
- de Lange EE, Mugler III JP, Brookeman JR, et al. Lung air spaces: MR imaging evaluation with hyperpolarized  $^3\text{He}$  gas. *Radiology* 1999; 210:851-857.
- Donnelly LF, MacFall JF, McAdams HP, et al. Cystic fibrosis: combined hyperpolarized  $^3\text{He}$ -enhanced and conventional proton MR imaging in the lung—preliminary observations. *Radiology* 1999; 212:885-889.
- Guenther D, Eberle B, Hast J, et al.  $^3\text{He}$  MRI in healthy volunteers: preliminary correlation with smoking history and lung volumes. *NMR Biomed* 2000; 13:182-189.
- Fichele S, Woodhouse N, Swift AJ, et al. MRI of helium-3 gas in healthy lungs: posture related variations of alveolar size. *J Magn Reson Imag* 2004; 20:331-335.
- Jinkins JR, Dworkin JS, Green AC, et al. Upright, weight-bearing, dynamic-kinetic MRI of the spine pMRI/kMRI. *Rivista Neuroradiol* 2002; 15:333-356.
- Jinkins JR, Dworkin JS, Green AC, et al. Upright, weight-bearing, dynamic-kinetic magnetic resonance imaging of the spine review of the first clinical results. *Rivista Neuroradiol* 2003; 16:55-74.
- Jinkins JR, Dworkin JS, Damadian RV. Upright, weight-bearing, dynamic-kinetic MRI of the spine: initial results. *Eur Radiol* 2005; 15:1815-1825.
- Tseng CH, Wong GP, Pomeroy VR, et al. Low-field MRI of laser polarized noble gas. *Phys Rev Lett* 1998; 81:3785-3788.
- Wong GP, Tseng CH, Pomeroy VR, et al. A system for low field imaging of laser-polarized noble gas. *J Magn Reson* 1999; 141:217-227.
- Mair RW, Hrovat MI, Patz S, et al.  $^3\text{He}$  lung imaging in an open access, very-low-field human magnetic resonance imaging system. *Magn Reson Med* 2005; 53:745-749.
- Ruset IC, Tsai LL, Mair RW, et al. A system for open-access He-3 human lung imaging at very low field. *Concepts Magn Reson B Magn Reson Eng* 2006; 29B:210-221.
- Parra-Robles J, Cross AR, Santyr GE. Theoretical signal-to-noise ratio and spatial resolution dependence on the magnetic field strength for hyperpolarized noble gas magnetic resonance imaging of human lungs. *Med Phys* 2005; 32:221-229.
- Durand E, Guillot G, Darrasse L, et al. CPMG measurements and ultrafast imaging in human lungs with hyperpolarized helium-3 at low field (0.1 T). *Magn Reson Med* 2002; 47:75-81.
- Owers-Bradley JR, Fichele S, Bennattayalah A, et al. MR tagging of human lungs using hyperpolarized He-3 gas. *J Magn Reson Imaging* 2003; 17:142-146.
- Venkatesh AK, Zhang AX, Mansour J, et al. MRI of the lung gas-space at very low-field using hyperpolarized noble gases. *Magn Reson Imaging* 2003; 21:773-776.
- Bidinosti CP, Choukeife J, Nacher PJ, et al. In vivo NMR of hyperpolarized  $^3\text{He}$  in the human lung at very low magnetic fields. *J Magn Reson* 2003; 162:122-132.
- Bidinosti CP, Choukeife J, Tastevin G, et al. MRI of the lung using hyperpolarized  $^3\text{He}$  at very low magnetic field (3 mT). *Magma* 2004; 16:255-258.
- West JB, Dollery CT, Naimark A. Distribution of blood flow in isolated lung; relation to vascular and alveolar pressures. *J Appl Physiol* 1964; 19:713-724.
- Frerichs I, Dudykevych T, Hinz J, et al. Gravity effects on regional lung ventilation determined by functional EIT during parabolic flights. *J Appl Physiol* 2001; 91:39-50.
- Williams MD, Murr PC. Laparoscopic insufflation of the abdomen depresses cardiopulmonary function. *Surg Endosc* 1993; 7:12-16.
- Druz WS, Sharp JT. Activity of respiratory muscles in upright and recumbent humans. *J Appl Physiol* 1981; 51:1552-1561.
- Behrakis PK, Baydur A, Jaeger MJ, et al. Lung mechanics in sitting and horizontal body positions. *Chest* 1983; 83:643-646.
- Barnas GM, Green MD, Mackenzie CF, et al. Effect of posture on lung and regional chest wall mechanics. *Anesthesiology* 1993; 78:251-259.
- Kolarzyk E, Szot WM, Lyszczarz J. Lung function and breathing regulation parameters during pregnancy. *Arch Gynecol Obstet* 2005; 272:53-58.

52. Fischer MC, Kadlecsek S, Yu J, et al. Measurements of regional alveolar oxygen pressure using hyperpolarized <sup>3</sup>He MRI. *Acad Radiol* 20005; 12:1430–1439.
53. Vidal Melo MF, Layfield D, Harris RS, et al. Quantification of regional ventilation-perfusion ratios with PET. *J Nucl Med* 2003; 44:1982–1991.
54. Rhodes CG, Valind SO, Brudin LH, et al. Quantification of regional V/Q ratios in humans by use of PET. I. Theory. *J Appl Physiol* 1989; 66:1896–1904.
55. Rhodes CG, Valind SO, Brudin LH, et al. Quantification of regional V/Q ratios in humans by use of PET. II. Procedure and normal values. *J Appl Physiol* 1989; 66:1905–1913.
56. Tulic MK, Christodouloupoulos P, Hamid Q. Small airway inflammation in asthma. *Respir Res* 2001; 2:333–339.
57. Hamid QA. Peripheral inflammation is more important than central inflammation. *Respir Med* 1997; 91(Suppl A):11–12.
58. Hamid Q, Song YL, Kotsimbos TC, et al. Inflammation of small airways in asthma. *J Allergy Clin Immunol* 1997; 100:44–51.
59. Poutler LW. Central inflammation is more important than peripheral inflammation. *Respir Med* 1997; 91(Suppl A):9–10.
60. Shaw RJ, Djukanovic R, Tashkin DP, et al. The role of small airways in lung disease. *Respir Med* 2002; 96:67–80.
61. Venegas JG, Winkler T, Musch G, et al. Self-organized patchiness in asthma as a prelude to catastrophic shifts. *Nature* 2005; 434:777–782.
62. Chan ED, Welsh CH. Geriatric respiratory medicine. *Chest* 1998; 114:1704–1733.
63. Johnson BD, Reddan WG, Pegelow DF, et al. Flow limitation and regulation of functional residual capacity during exercise in a physically active aging population. *Am Rev Respir Dis* 1991; 143:960–967.
64. Hazzard WR. *Principles of geriatric medicine and gerontology*, 5th ed. New York, NY: McGraw-Hill Professional, 2003.
65. enhamou D, Muir JF, Melen B. Mechanical ventilation in elderly patients. *Monaldi Arch Chest Dis* 1998; 53:547–551.
66. Barst RJ, McGoon M, Torbicki A, et al. Diagnosis and differential assessment of pulmonary arterial hypertension. *J Am Coll Cardiol* 2004; 43:40S.
67. Fedullo PF, Auger WR, Kerr KM, et al. Chronic thromboembolic pulmonary hypertension. *N Engl J Med* 2001; 345:1465–1472.
68. Fedullo PF, Auger WR, Moser KM, et al. Hemodynamic response to exercise in patients with chronic, major vessel thromboembolic pulmonary hypertension. *Am Rev Respir Dis* 1990; 141:A890.
69. Tsai LL, Mair RW, Rosen MS, et al. An open-access, very-low-field MRI system for posture-dependent <sup>3</sup>He human lung imaging. *J Magn Reson*. In press.
70. Morgan PS, Conolly S, Mazovski A. Design of uniform field biplanar magnets. *Proc 5th Meeting ISMRM*. 1997; 1447.
71. Yablonskiy DA, Sukstanskii AL, Ackerman JH. Image artifacts in very low magnetic field MRI: The role of concomitant gradients. *J Magn Reson* 2005; 174:279–286.
72. Zhao L, Mulkern R, Tseng CH, et al. Gradient echo imaging considerations for hyperpolarized <sup>129</sup>Xe MR. *J Magn Reson B* 1996; 113:179–183.
73. Kim YR, Reborek KJ, Schmainda KM. Water exchange and inflow affect the accuracy of T1-GRE blood volume measurements: implications for the evaluation of tumor angiogenesis. *Magn Reson Med* 2002; 47:1110–1120.
74. Wild JM, Woodhouse N, Paley MNJ, et al. Comparison between 2D and 3D gradient-echo sequences for MRI of human lung ventilation with hyperpolarized <sup>3</sup>He. *Magn Reson Med* 2004; 52:673–678.
75. Wild JM, Fischele S, Woodhouse N, et al. 3D volume-localized pO<sub>2</sub> measurement in the human lung with <sup>3</sup>He MRI. *Magn Reson Med* 2005; 53:1055–1064.
76. Kadlecsek SJ, Emami K, Fischer MC, et al. Imaging physiological parameters with hyperpolarized gas MRI. *Prog Nucl Magn Reson Spectrosc* 2005; 47:187–212.
77. Callaghan PT. *Principles of Nuclear magnetic resonance microscopy*. Oxford, UK: Oxford University Press, 1991.